



Micrometeorological determinants of pedestrian thermal exposure during record-breaking heat in Tempe, Arizona: Introducing the MaRTy observational platform



Ariane Middel^{a,b}, E. Scott Krayenhoff^{b,c,*}

^a School of Arts, Media and Engineering (AME), School of Computing, Informatics, and Decision Systems Engineering (CIDSE), Arizona State University, 950 S. Forest Mall, Stauffer B, Tempe, AZ 85281, USA

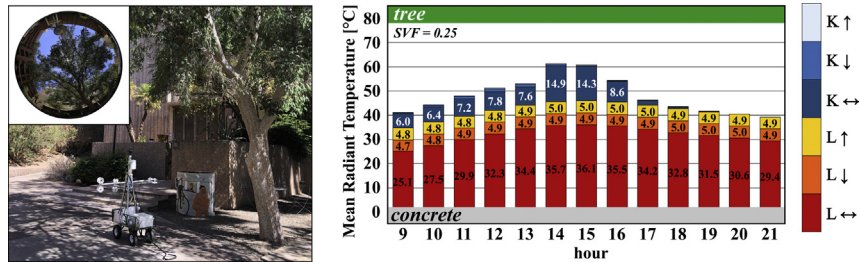
^b Urban Climate Research Center, Arizona State University, 975 S Myrtle Ave, Tempe, AZ 85281, USA

^c School of Environmental Sciences, University of Guelph, 50 Stone Road East, Guelph, ON N1G 2W1, Canada

HIGHLIGHTS

- Health impacts from heat exposure relate to urban design and ambient weather.
- A cart with 12 radiation sensors (MaRTy) measures human exposure to extreme heat.
- Heat exposure variability is from lateral inputs of longwave and shortwave radiation.
- Shade, ground vegetation and cool vertical surfaces together create additive cooling.
- Adaptation to future urban heat depends on radiant cooling of pedestrian spaces.

GRAPHICAL ABSTRACT



ARTICLE INFO

Article history:

Received 11 February 2019

Received in revised form 21 May 2019

Accepted 5 June 2019

Available online 7 June 2019

Editor: SCOTT SHERIDAN

Keywords:

Extreme heat

Mean radiant temperature

Thermal comfort

MaRTy

Radiation budget decomposition

Microscale Urban Design

ABSTRACT

We report the first set of urban micrometeorological measurements for assessment of pedestrian thermal exposure during extreme heat in a dry climate. Hourly measurements of air temperature, humidity, wind speed and six-directional shortwave and longwave radiation were recorded with a mobile human-biometeorological station (MaRTy) from 10:00 to 21:00 local time, June 19, 2016, at 22 sites that include diverse microscale urban land cover. Sky view factor (SVF) and 360° pervious and impervious view factors for each location were calculated from six-directional fisheye photographs. Mean radiant temperature (T_{MRT}) was determined using the six-directional method. Three-dimensional radiation budgets were decomposed into directional weighted shortwave and longwave radiation components to create a distinct T_{MRT} profile for each site and determine the main drivers of T_{MRT} and thermal exposure. Air temperature peaked locally at 48.5 °C, with a maximum T_{MRT} of 76.4 °C at 15:00 MST in an east-west building canyon. Longwave radiation measured by laterally-oriented sensors dominated the T_{MRT} budget, suggesting the importance of cooling vertical surfaces adjacent to pedestrians. Lateral shortwave radiation contributions were most spatially and temporally variable across T_{MRT} profiles, reflecting the diverse shade conditions. The largest radiation fluxes contributing to T_{MRT} were particularly sensitive to shade and secondarily to ground cover. Trees reduced afternoon T_{MRT} up to 33.4 °C but exhibited a clear T_{MRT} increase of up to 5 °C after sunset; during daytime, trees generated ground cover-dependent longwave radiant cooling or warming. Replacement of impervious with pervious ground cover cooled T_{MRT} at all measurement times, even under dense tree shade. While recent work has found that adaptation cannot offset projected

* Corresponding author at: School of Environmental Sciences, University of Guelph, 50 Stone Road East, Guelph, ON N1G 2W1, Canada.
E-mail addresses: ariane.middel@asu.edu (A. Middel), skrayenh@uoguelph.ca (E.S. Krayenhoff).

urban air temperature increases, outdoor thermal exposure depends on additional micrometeorological variables, including shortwave and longwave radiation, indicating the need and the opportunity to create pedestrian spaces that are radiantly cool within the context of future urban heat.

© 2019 The Authors. Published by Elsevier B.V. This is an open access article under the CC BY-NC-ND license (<http://creativecommons.org/licenses/by-nc-nd/4.0/>).

1. Introduction

The world's climate is warming (IPCC, 2014), and extreme heat events are projected to increase in frequency, duration, and intensity (Meehl and Tebaldi, 2004). Concurrently, rapid urban development is underway globally and is projected to continue (Bierwagen et al., 2010), adding to urban heat (Oke, 1982; Argüeso et al., 2014; Georgescu et al., 2014; Krayenhoff et al., 2018). These combined drivers of urban warming (i.e., climate change and urbanization) are projected to result in up to 40 (70) additional extreme heat afternoons (nights) per year across much of the contiguous U.S. by the end of the 21st century under Representative Concentration Pathway (RCP) 8.5, which assumes continuous, heavy use of fossil fuels (Krayenhoff et al., 2018). At the same time, the urban population is aging; by 2035, one in every five Americans will be retirement age, and older adults will outnumber children (Vespa et al., 2018). This demographic change, combined with urban migration and warming, will collectively lead to increased exposure of vulnerable populations to greater extremes of heat with higher frequency. Moreover, urban development is proceeding more rapidly in most areas of the world relative to the U.S., much of it in dryland regions whose future climates are also more likely to include more extreme temperatures (Bucchignani et al., 2018; Lazzarini et al., 2015; Seto et al., 2011).

Excessive heat has myriad impacts in the human realm. In Arizona, extreme heat leads to nearly 2000 emergency room visits and >100 deaths every year (ADHS, 2018). Contemporary summer heat waves in hot desert cities could soon become the new normal for those cities; at the same time, they may give insight into the extremes of future heat wave conditions in more temperate climates and serve as testbeds to evaluate potential heat mitigation strategies (Hondula et al., 2019). Studies show that extreme heat leads to increased human morbidity and mortality (Luber and McGeehin, 2008; Basu, 2009; Gosling et al.,

2009; USGCRP, 2018), larger energy and water demands for cooling and irrigation (Miller et al., 2008; Zuo et al., 2015), reduced physical activity (Tucker and Gilliland, 2007), and increased thermal stress (Harlan et al., 2006; Parsons, 2014).

Although biometeorology in cities is a growing research field internationally (Hondula et al., 2017), little is known about the impact of the built environment on human heat stress and outdoor thermal comfort under extreme heat conditions. Outdoor thermal comfort has been assessed for a range of conditions, including moderate to high heat (Lee et al., 2014; Middel et al., 2016), but more observational studies are needed to examine conditions that induce extreme heat stress for most of the day and to identify key drivers of outdoor thermal exposure and associated opportunities for adaptation.

Outdoor human thermal exposure is highly spatially variable and requires microscale assessment, because air temperature alone does not fully capture the variability of the thermal conditions experienced in urban environments. Exposure to thermally uncomfortable conditions depends on several micrometeorological factors in addition to air temperature, including shortwave and longwave radiation, wind speed, and humidity. Wind speed is typically low during extreme heat events, reducing convective cooling, and radiation dominates thermal comfort, especially in hot and dry environments (Mayer and Höppe, 1987; Thorsson et al., 2007; Lindberg et al., 2008; Shashua-Bar et al., 2011; Johansson et al., 2014; Middel et al., 2014; Middel et al., 2016). In this context, mean radiant temperature (T_{MRT}) has emerged as important determinant of thermal comfort. T_{MRT} is the “uniform temperature of an imaginary enclosure in which the radiant heat transfer from the human body equals the radiant heat transfer in the actual non-uniform enclosure” (ISO, 1998) and can be measured using pyranometers and pyrgeometers that are arranged in six directions or, more conveniently but less accurately, with a globe thermometer (Thorsson et al., 2007). T_{MRT} is also a key component of thermo-physiological stress indices, such as Physiologically Equivalent Temperature (PET) (Höppe, 1999) and the Universal Thermal Climate Index (UTCI) (Jendritzky et al., 2012; Bröde et al., 2012). As an integral measure of radiative flux densities, T_{MRT} helps capture fine-scale thermal variations between sites but cannot resolve the different micrometeorological contributions of urban surfaces and their relative importance. Assessing the effects of specific urban form and design features on radiative fluxes that pedestrians are exposed to is a requirement for understanding the drivers of T_{MRT} variation. Only then can urban heatscapes be efficiently transformed into more comfortable outdoor spaces through climate-sensitive urban design.

Several studies have observed and modeled the directional components of 3D flux radiation densities to understand the impact of individual urban form and design elements on human outdoor thermal exposure and comfort (Ali-Toudert and Mayer, 2007; Holst and Mayer, 2011; Lindberg and Grimmond, 2011; Lindberg et al., 2014; Lee et al., 2014; Kántor et al., 2016, 2018; Lai et al., 2018). Here, for the first time, we decompose six-directional T_{MRT} observations of an extreme heat day to isolate individual radiative contributions from sky (sky view factor, SVF) as well as pervious and impervious land cover, both sunlit and shaded, and quantitatively assess the relative magnitudes of each micrometeorological contribution to the pedestrian thermal environment and associated exposure. Based on our analysis, we recommend optimal microscale heat mitigation design strategies for extreme temperature conditions in hot, dry urban climates.

List of symbols and acronyms

a_k	absorption coefficient for shortwave radiation
a_l	absorption coefficient for longwave radiation
BVF	building view factor
K_i	incident shortwave radiation from direction i (150° field of view), $W\ m^{-2}$
L_i	incident longwave radiation from direction i (150° field of view), $W\ m^{-2}$
RH	relative humidity, %
PET	Physiologically Equivalent Temperature, $^\circ C$
SVF	sky view factor
T_a	air temperature, $^\circ C$
T_{MRT}	mean radiant temperature, $^\circ C$
T_s	ground surface temperature, $^\circ C$
UTCI	Universal Thermal Climate Index, $^\circ C$
v	wind speed, $m\ s^{-1}$
VVF	vegetation view factor
W_i	Angular weighting factor for standing reference person for radiation incident from direction i

2. Methods

2.1. Study area

Tempe, Arizona (33.4294° N, 111.9431° W) is located in the East Valley of the Phoenix metropolitan area in the Southwestern U.S. Typical of the Sonoran Desert, Tempe's climate is semi-arid with an average annual rainfall of only 237-mm and average high temperature above 39.4 °C during the summer months (Western Regional Climate Center, 2018).

While the southern parts of the city are lower density residential neighborhoods (Local Climate Zone 6, open lowrise), strip malls (Local Climate Zone 8, large lowrise), and office parks (Local Climate Zone 5, open midrise), the northern parts are currently undergoing rapid densification. The growing skyline is transitioning from open lowrise/midrise to open midrise/highrise, with several new apartment complexes and hotels under construction. Our observational field campaign was conducted on Arizona State University's main campus, which is in the northern part of Tempe, just south-east of the Mill Avenue District, a popular shopping and entertainment area. The campus is a 2.6-km² agglomeration of broad interconnected pedestrian malls and can be classified as open midrise (Fig. 1).

2.2. Observations

We conducted hourly microclimate transects at ASU's Tempe campus on June 19, 2016, a clear, hot, pre-monsoon summer day. It was

the hottest day of the year for Tempe, with record-breaking 47.8 °C maximum daily temperature at the local airport (see Section 3.1). Hourly observations were collected between 09:00 MST and 21:00 MST using a custom-built mobile human-biometeorological platform (MaRTy, Fig. 2). The cart recorded location (lat/lon [°]), air temperature (T_a [°C]); relative humidity (RH [%]); wind speed (v [m s⁻¹]); and longwave (L_i [W m⁻²]) and shortwave (K_t [W m⁻²]) radiant flux densities in a 6-directional setup (Höppe, 1992; Ali-Toudert and Mayer, 2007). Transects were 45-min in duration and were conducted at walking speed along the 22 locations illustrated in Fig. 1, included a 45-s stop at each location to account for sensor lag (Håb et al., 2015). Observations were logged at 2-s intervals. Sampled locations include a matrix of combined surface ground cover (grass, concrete, asphalt, gravel), site albedos (0.16–0.39), and shade types (artificial shade, natural shade, partial shade) to cover a wide range of microclimatic environments (Table 1). To characterize the surroundings in the net radiometers' field of view at each site, fisheye photos were taken at 1.1-m height with a Canon EOS 6D and Canon EF 8–15-mm f/4 Fisheye USM Ultra-Wide Zoom lens facing upwards (hemispherical view) and in each cardinal direction (lateral view). Due to the manual intensity and potential health risks of operating MaRTy during these extreme heat conditions, the observational data set is limited to one 12-hour period. For example, even with the majority of our time spent in air-conditioned spaces during the experiment (1 h 10 min each out of every 2 h period), it was not possible to maintain hydration with water alone – substantial consumption of sports drinks for the added electrolytes was required.



Fig. 1. Study area and fisheye photos of study sites on Arizona State University's main campus in Tempe, AZ, USA. A variety of microclimates with different ground surface cover and shade combinations are represented.

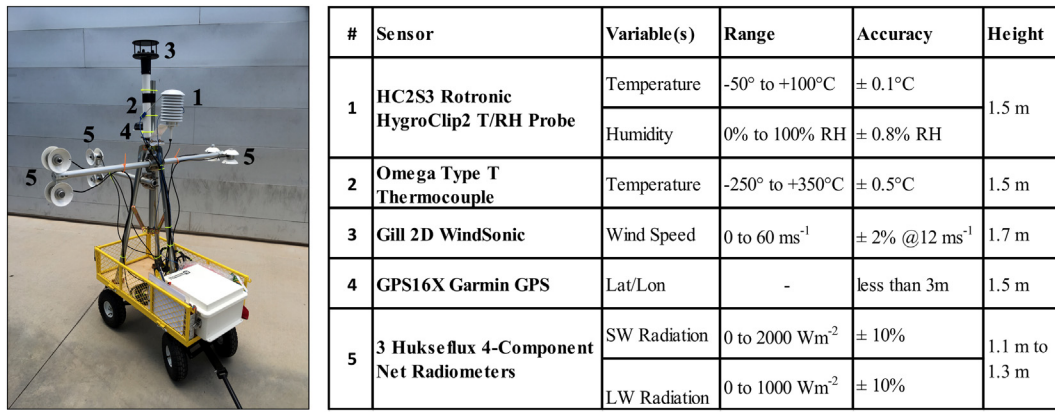


Fig. 2. Mean radiant temperature cart *MaRTy* with six-directional setup (left); sensor specifications (right).

2.3. Data processing

Only the stationary *MaRTy* observations at the selected 22 locations were considered in the analysis. The first 10 and last 5 records (20-s and 10-s, respectively) at each transect stop were discarded to account for the sensors' response time and to minimize net radiometer interference when the cart operator approached the instrumentation to continue the transect. The remaining records for each stop were averaged and then time-detrended to the turn of the hour for cross-site comparison using a polynomial fit through all hourly measurements at the specific location. T_{MRT} [°C] was calculated from the processed 6-directional K_i and

L_i observations at each location applying angular factors W_i for a standing reference person (Höppe, 1992; VDI, 1998):

$$T_{MRT} = \sqrt[4]{\frac{\sum_{i=1}^6 W_i (a_k K_i + a_l L_i)}{a_l \cdot \sigma}} - 273.15 \text{ K} \quad (1)$$

where $a_k = 0.70$ and $a_l = 0.97$ are the absorption coefficients for shortwave and longwave radiant flux densities, σ is the Stefan-Boltzmann constant, $W_i = 0.06$ for the up and down facing sensors, and $W_i = 0.22$ for the sensors pointing in each cardinal direction. Based on the processed T_{MRT} , T_a , RH , and v observations, we calculated the thermal comfort indices *PET* (Höppe, 1999) and *UTCI* (Jendritzky et al., 2012) for each location and hour. Indices were calculated for a 35-year old 1.7 m standing male with a clothing resistance of 0.5 clo. To assess the directional contributions of radiant flux densities on thermal comfort, we decomposed T_{MRT} into its weighted shortwave and longwave radiation components for the lateral, up, and down facing sensors, creating a distinct profile of diurnally-varying contributions to T_{MRT} for each location. In other words, we assess weighted shortwave and longwave radiation fluxes from the following three incoming directions separately: upward (one pyranometer and one pyrgeometer), downward (one pyranometer and one pyrgeometer), and laterally (four pyranometers and four pyrgeometers).

Site-specific 360° urban environment characteristics were derived through manual segmentation of fisheye photos into impervious, pervious, and sky pixels (Fig. 3). For the upper hemisphere photos, we calculated the sun duration for June 19, 2016, the 180° sky view factor (SVF), building view factor (BVF), and vegetation view factor (VVF) using a modified version of the Steyn (1980) method (Middel et al., 2017; Middel et al., 2018). For the four lateral fisheye photos at each site, we calculated average view factors of the sky, impervious, and pervious surfaces to determine the 360° SVF, BVF, and VVF. We then grouped the sites into high SVF (0.66–1.00), medium SVF (0.33–0.65), low SVF (0.00–0.32) mainly obstructed by vegetation, and low SVF mainly obstructed by buildings (Fig. 4).

3. Results

3.1. Meteorological observations

Field observations were conducted in Tempe on the hottest day of the year locally, June 19, 2016, with air temperature reaching record-breaking 47.8 °C at nearby Phoenix Sky Harbor International Airport (Table 2). At 7.3 °C above the June 19 daily mean, June 19, 2016 broke the previous record of 46.1 °C, set in 1968, and became the day with the fifth-highest temperature ever recorded at Sky Harbor. The National Weather Service issued an excessive heat warning for several days. High

Table 1

Summary of transect stop characteristics: ground cover, site albedo, shade type, transmissivity of tree crowns (daytime average), sky view factor (SVF), and daily sun duration on June 19, 2016.

ID	Surface type	Site albedo	Shade type	Tree transmissivity ^a	SVF	Sun duration 6/19 [h]
1	Asphalt	0.16	–	–	0.94	13.0
2	Concrete	0.25	Tunnel	–	0.01	0.6
3	Concrete	0.25	Tree (<i>Ulmus parvifolia</i>)	0.106	0.25	2.8
4	Concrete	0.23	–	–	0.55	10.4
5	Concrete	0.30	–	–	0.80	12.2
6	Concrete	0.38	Tree (<i>Prosopis glandulosa</i>)	0.522	0.35	6.2
7	Concrete	0.20	–	–	0.84	11.8
8	Concrete	0.23	Tree (<i>Quercus virginiana</i>)	0.650	0.52	5.0
9	Grass	0.39	Tree (<i>Pinus canariensis</i>)	0.024	0.06	0.6
10	Concrete	0.28	–	–	0.86	11.0
11	Grass	0.26	–	–	0.87	11.2
12	Concrete	0.23	–	–	0.71	9.0
13	Concrete	0.23	Solar canopy	–	0.14	2.0
14	Grass (dry)	0.32	–	–	0.82	11.2
15	Grass	0.26	Tree (<i>Quercus virginiana</i>)	0.054	0.11	1.4
16	Concrete	0.26	–	–	0.64	9.4
17	Concrete	0.23	Tree (<i>Ficus nitida</i>)	0.031	0.05	0.8
18	Concrete	0.23	Tree (<i>Quercus virginiana</i>)	0.360	0.46	4.4
19	Concrete	0.23	–	–	0.78	10.6
20	Concrete	0.22	–	–	0.50	11.0
21	Concrete	0.23	N/S canyon	–	0.29	5.2
22	Concrete	0.20	Tunnel	–	0.01	0.6

^a Transmissivity values derived based on measurements on June 19, 2016, and based on cart radiation measurements intended for thermal exposure assessment as opposed to radiation sensor placement in optimal location for transmissivity measurement (e.g., on north side of tree trunk).

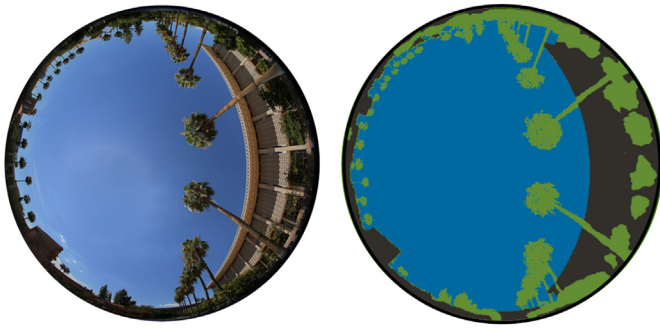


Fig. 3. Upper hemisphere fisheye photo and corresponding manual segmentation into sky, building, and vegetation pixels.

pressure meteorological conditions were stable for several days before and after, albeit with lower maximum temperatures that still reached 44 °C.

During our transects on Arizona State University's main campus, T_a peaked at 48.5 °C on an open (SVF = 0.71), sun-exposed concrete walkway (location 12, Table 3). The lowest T_a peak (45.6 °C) occurred in a concrete tunnel that cuts through a building. The tunnel also had the lowest T_{MRT} maximum with 39.7 °C, while T_{MRT} reached a daily high of 76.4 °C in an E-W building canyon with bright concrete and the majority of walls sunlit (location 20). As expected, the lowest peak ground surface temperature (T_s) across all sites was recorded on grass under dense tree cover (36.7 °C, location 9), and the highest peak T_s was found on an exposed asphalt parking lot (location 1) at 65.8 °C, which had the lowest albedo (Table 1). Wind speed was generally low, with peak gusts of up to 3.0 m s⁻¹ inside building tunnels, but <1.0 m s⁻¹ on average across all sites and times of day. After sunset, T_{MRT} was highest in a narrow north-south canyon framed by concrete walls (41.4 °C, location 21) and lowest on an open grass field (28.9 °C, location 11).

3.2. Thermal stress indices and comfort implications

The $UTCI$ and PET indices are chosen to characterize variation of thermal exposure of a standing person as a function of measured micrometeorology across the measurement locations and over the observational period (11:00–21:00 MST). Hourly $UTCI$ peaked at 54.5 °C, whereas PET

reached 66.0 °C, both in the E-W oriented canyon where T_{MRT} peaked (Section 3.1); this canyon had a concrete floor and walls and height-to-width ratios of 1.2 (north) and 1.6 (south; location 20; Table 3). Median $UTCI$ and PET across all sites during the measurement period were 44.2 °C and 49.9 °C, respectively. Although both equivalent temperature indices, PET was 4.3 °C higher than $UTCI$ in the median, and for concrete locations in the afternoon sunlight, PET was ≈10 °C greater than $UTCI$, probably due to the enhanced sensitivity to T_{MRT} of PET relative to $UTCI$ for these conditions (Fig. 5b).

The indices suggest afternoon thermal comfort was best in grassy locations with trees providing shade (locations 9 and 15; Table 3). During evening hours an extensive open grassy area was most comfortable (location 11), and areas proximate to trees and grassy areas were cooler than average (locations 8–10, 14–16). Locations directly under trees, exhibiting low SVF and large VVF, had evening $UTCI$ and PET that were 1–2 °C higher than adjacent locations with larger sky views (locations 9 vs. 11, 17 vs. 16). Notably, grass lowered $UTCI$ and PET relative to concrete at all measurement times, even when completely shaded (locations 9 vs. 17). Concrete canyons and open asphalt yielded the least comfortable daytime conditions, and asphalt remained warmest into the evening. Tunnels under buildings were among the best locations for daytime thermal comfort and among the worst for evening thermal comfort (locations 2 and 22). They also exhibited higher wind speeds than most other locations. $UTCI$ and PET varied by a maximum of 12.9 °C and 23.2 °C between measurement locations (at 15:00 MST), respectively, whereas they ranged by 17.0 °C and 27.8 °C over the course of the measurement period at the most variable site (location 10, concrete sidewalk amidst an open grass field).

For these hot and dry conditions, both indices were most sensitive to T_a (Fig. 5). PET exhibited a similarly strong sensitivity to T_{MRT} , whereas $UTCI$ was about half as sensitive to T_{MRT} as T_a (Fig. 5a, b). Both indices had negligible sensitivity to relative humidity and wind speed, suggesting that thermal comfort during extreme heat conditions in Phoenix is dominated by T_a , T_s , and exposure to direct solar radiation. T_{MRT} explained 70% of $UTCI$ variation and 90% of PET variation, spanning the measurement sites and observation period (Fig. 5e). T_{MRT} varied by 35–40 °C between measurement locations during mid-afternoon, and by a similar magnitude over the 11:00–21:00 MST measurement period at locations with direct solar exposure. T_a , by contrast, varied no more than 4.4 °C across the measurement locations at any given hour, and varied by <9 °C over the measurement period in any given location. Hence, though $UTCI$ and PET are more sensitive to T_a than T_{MRT} , the higher spatial and temporal variation of T_{MRT} in our measurements

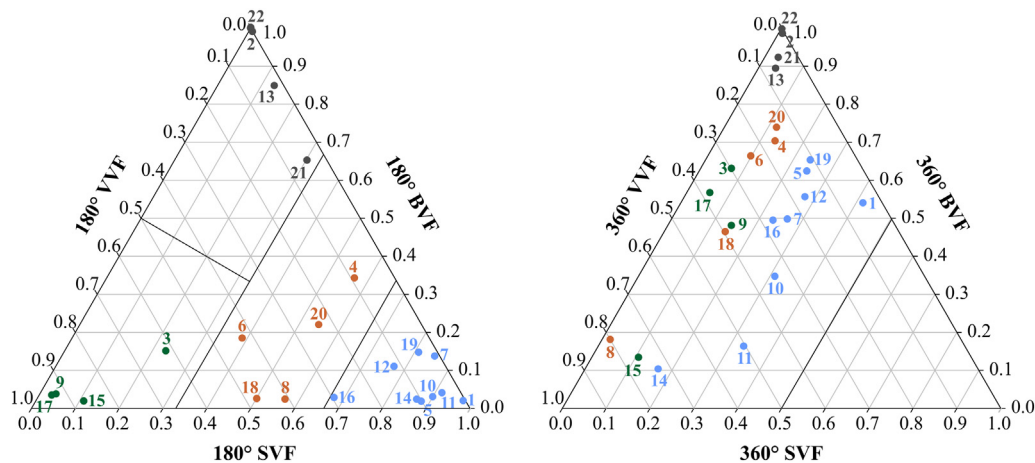


Fig. 4. Segmentation of upper hemisphere (180°) and sphere (360°) into sky view factor (SVF), building view factor (BVF), and vegetation view factor (VVF); sites grouped into high SVF (blue), medium SVF (brown), low SVF mainly obstructed by vegetation (green), and low SVF mainly obstructed by buildings (grey).

Table 2
Comparison of daily and monthly climate normals (Western Regional Climate Center, 2018) to MaRTy cart observations.

	Tempe Arizona State University Station			Phoenix Sky Harbor Station			MaRTy Cart
	June (monthly average)	June 19 (daily average)	June 19, 2016	June (monthly average)	June 19 (daily average)	June 19, 2016	June 19, 2016
Maximum temperature [°C]	39.3	39.7	47.2	39.9	40.5	47.8	48.5
Record high daily temperature [°C]	48.3° (1970)	47.2° (1968)	–	50.0° (1990)	46.1° (1968)	–	–
Minimum temperature [°C]	19.8	22.3	28.3	25.4	25.9	29.4	–
Precipitation [mm]	0.762	0.051	0.000	0.508	0.051	0.000	0.000

rendered it a better predictor of the spatio-temporal variability of the thermal exposure of a standing reference person in these outdoor spaces.

3.3. Controls on T_{MRT} variation

The dominant influence of T_{MRT} on the spatio-temporal variability of $UTCI$ and PET for the observed conditions invites further analysis of this compound variable. The 6-directional shortwave and longwave radiation measurements are separated into six constituents: upward shortwave/longwave, downward shortwave/longwave, and lateral shortwave/longwave, where the lateral components are means of the four lateral-facing sensors. Moreover, lateral components are weighted more heavily compared to up- and down-facing components to account for realistic geometrical exposure of the standing human body (Section 2.3).

Apart from select morning hours, lateral components of the longwave flux are the largest contribution to pedestrian T_{MRT} for all measurement locations and times (Figs. 6 & 7). The lateral longwave flux depends on vertical surfaces (walls) and tall vegetation (trees) in addition to ground cover and sky exposure, suggesting that addition of cool surfaces (e.g., evaporating, shaded or thermally conservative surfaces) in sun-exposed areas adjacent to pedestrian walkways may result in strong reductions in T_{MRT} and consequently $UTCI$ and PET . Lateral shortwave radiation flux is primarily unidirectional in origin (for clear sky conditions) and as a consequence it is typically smaller than lateral longwave radiation. It is also more variable spatially and temporally and is responsible for the largest variations in T_{MRT} (Fig. 6) – in accordance with evidence that shade is key to thermal comfort amelioration during hot daytime conditions (Middel et al., 2016). Notably, lateral

(downward) shortwave flux drops (increases) around midday due to low solar zenith angle ($\approx 10^\circ$), leading to a dip in overall T_{MRT} .

Myriad clues to the influence of microscale urban design on T_{MRT} appear in Fig. 6. While a solar photovoltaic canopy (location 13) and dense trees (location 17) both provide near-complete shade, total T_{MRT} is 3 °C higher with the former near noon, 1 °C greater in the late afternoon and indistinguishable after sunset; increased downwelling and lateral longwave radiation components are the cause, probably due to the higher temperature of the photovoltaic panels compared to tree foliage. Presumably this difference would be larger for a solar canopy located closer to pedestrians (the location 13 solar canopy is at approximately 7.5-m).

Open areas with concrete and asphalt ground cover (locations 1 and 7) have a 44.3 °C contribution to T_{MRT} from upwelling and lateral longwave flux at 14:00 MST, a contribution that is 4.6 °C lower for dry grass (location 14) and 11.5 °C lower for irrigated grass (location 11; Table 3; Fig. 6). This discrepancy persists to 21:00 MST with about half the magnitude, partially explaining why location 11 exhibits the lowest evening $UTCI/PET$. Furthermore, the effect of ground cover remains apparent directly under dense tree cover, where the T_{MRT} contribution of upwelling and lateral longwave radiation over grass (location 9) is 3.9 °C lower than concrete (location 17) at 14:00 MST and 3.2 °C lower at 21:00 MST. Trees increase the longwave contribution to T_{MRT} at all times of day over grass (location 9 vs. 11; Fig. 6), and in the evening over concrete, but they reduce it over concrete during the day (locations 7 or 16 vs. 17; Figs. 6 and 7). Trees exert both a warming impact on the longwave component of T_{MRT} by blocking the cool sky (Krayenhoff et al., 2014) as well as a cooling effect by shading and therefore cooling the ground surface; because unshaded concrete is much warmer than unshaded grass, the longwave warming impact of trees is smaller than

Table 3
Summary of site descriptors and MaRTy cart observations for selected times of day: 11:00–21:00 average, peak values, and after sunset (21:00 MST).

ID	surface type	shade type	SVF	BVF	VVVF	lateral FOV (sky)	lateral FOV (impervious)	lateral FOV (pervious)	sun dur [h]	11:00 h - 21:00 h average										daytime peak										21:00 h (after sunset)									
										MRT [°C]	T _{air} [°C]	T _{surf} [°C]	T _{sky} [°C]	RH [%]	v [m/s]	PET [°C]	UTCI [°C]	MRT [°C]	T _{air} [°C]	T _{surf} [°C]	T _{sky} [°C]	RH [%]	v [m/s]	PET [°C]	UTCI [°C]	MRT [°C]	T _{air} [°C]	T _{surf} [°C]	T _{sky} [°C]	PET [°C]	UTCI [°C]								
1	asphalt	-	0.938	0.030	0.032	0.417	0.539	0.044	13.0	61.4	45.4	57.7	21.9	6.8	1.9	56.8	48.7	74.1	47.8	65.8	22.9	11.1	2.8	65.0	54.1	35.4	42.4	44.1	21.5	41.5	40.1								
2	concrete	tunnel	0.010	0.990	0.000	0.010	0.985	0.005	0.6	38.8	44.4	38.9	40.3	7.2	1.8	45.5	42.4	40.8	46.8	40.4	42.3	11.6	3.1	50.6	45.1	39.7	41.6	39.0	41.3	43.3	40.6								
3	concrete	tree	0.246	0.158	0.596	0.072	0.630	0.298	2.8	49.0	44.2	43.8	39.8	7.1	1.6	49.7	44.5	61.4	46.3	47.8	41.7	10.7	2.7	55.9	48.5	39.2	42.0	40.5	37.0	42.9	40.5								
4	concrete	-	0.547	0.349	0.105	0.135	0.702	0.163	10.4	62.3	44.9	55.1	30.5	7.5	0.9	56.2	48.2	74.5	47.4	62.0	31.9	11.6	1.5	64.6	53.6	38.2	41.0	43.7	28.7	40.4	38.9								
5	concrete	-	0.804	0.146	0.051	0.247	0.623	0.130	12.2	62.3	45.8	56.2	25.2	7.4	0.7	56.3	48.4	75.6	47.9	63.4	26.8	11.6	1.4	65.4	54.0	36.9	40.9	44.7	23.3	39.2	38.2								
6	concrete	tree	0.351	0.190	0.459	0.099	0.663	0.238	6.2	57.9	44.9	51.8	34.1	7.0	1.1	53.9	47.1	73.9	47.6	59.7	36.5	11.1	2.0	64.0	53.5	39.0	40.3	44.3	30.7	40.4	38.5								
7	concrete	-	0.839	0.020	0.141	0.266	0.497	0.237	11.8	59.4	44.9	55.8	23.8	7.8	0.9	54.5	47.3	73.8	47.6	63.6	25.0	11.8	1.5	64.4	53.6	35.9	40.4	43.2	22.5	38.4	37.6								
8	concrete	tree	0.516	0.026	0.457	0.020	0.180	0.800	5.0	55.1	44.1	48.9	31.7	7.7	0.6	51.5	45.3	71.0	47.4	55.1	33.6	11.0	0.8	62.2	51.7	36.3	39.3	41.2	29.2	38.3	36.8								
9	grass	tree	0.055	0.040	0.904	0.147	0.480	0.373	0.6	40.3	43.7	35.2	42.9	8.2	0.4	42.9	41.1	43.0	46.3	36.7	46.3	12.9	1.2	47.3	44.0	35.5	39.7	32.9	38.9	37.3	36.7								
10	concrete	-	0.865	0.033	0.102	0.313	0.346	0.341	11.0	58.6	44.3	50.4	23.0	8.2	0.8	53.6	46.5	72.7	47.5	57.5	24.4	12.9	1.5	63.9	53.2	31.7	39.6	38.5	21.8	36.1	36.2								
11	grass	-	0.873	0.044	0.083	0.333	0.162	0.504	11.2	55.8	44.6	38.7	23.0	8.6	0.9	52.5	46.1	69.4	47.8	43.1	24.4	12.3	1.4	61.8	51.9	28.9	39.8	30.0	21.7	35.2	35.8								
12	concrete	-	0.714	0.116	0.170	0.276	0.556	0.168	9.0	58.4	45.2	53.2	26.4	7.6	0.9	54.4	47.3	74.5	48.5	60.3	27.9	12.3	2.4	65.2	54.1	35.3	40.8	42.0	24.9	38.6	38.0								
13	concrete	sol. canopy	0.144	0.730	0.126	0.041	0.893	0.066	2.0	46.5	44.7	45.3	46.5	7.4	0.6	47.2	43.6	51.1	47.6	47.7	31.6	11.3	1.3	51.7	46.9	39.0	41.1	40.8	37.2	40.1	38.7								
14	grass (dry)	-	0.816	0.025	0.159	0.168	0.102	0.729	11.2	51.5	44.6	45.3	28.9	7.9	0.6	49.7	44.8	69.4	47.4	55.8	30.6	12.1	1.2	60.8	50.6	32.7	40.5	33.3	26.6	36.6	36.8								
15	grass	tree	0.111	0.030	0.859	0.108	0.133	0.759	1.4	44.8	44.3	37.0	42.1	7.7	0.6	46.1	42.9	54.9	47.1	40.0	44.9	11.5	1.3	52.7	46.9	35.4	39.9	33.0	37.6	37.9	37.0								
16	concrete	-	0.636	0.031	0.332	0.235	0.494	0.271	9.4	58.9	44.7	54.7	24.1	7.8	0.6	53.9	46.8	71.7	47.7	62.7	25.5	12.0	1.2	62.8	52.9	35.4	39.9	42.4	22.4	37.9	37.1								
17	concrete	tree	0.045	0.038	0.917	0.054	0.566	0.379	0.8	45.0	44.5	42.3	43.3	8.0	0.7	46.5	43.2	48.6	47.3	44.6	45.9	12.9	1.2	50.3	46.1	38.8	40.3	39.9	39.1	39.7	38.2								
18	concrete	tree	0.465	0.027	0.508	0.141	0.464	0.396	4.4	50.8	44.8	48.2	32.3	7.8	0.8	49.8	44.9	65.6	47.6	57.2	34.3	12.5	1.4	58.9	50.1	37.6	40.9	41.4	29.6	39.3	38.4								
19	concrete	-	0.779	0.153	0.068	0.240	0.652	0.108	10.6	58.6	44.6	55.6	25.2	7.2	0.5	53.5	46.6	75.9	47.2	65.0	26.7	11.4	1.1	65.3	52.8	36.0	40.1	41.7	23.3	37.8	37.3								
20	concrete	-	0.505	0.230	0.265	0.121	0.738	0.141	11.0	61.8	45.0	56.1	30.7	7.5	1.1	56.6	48.5	76.4	47.9	64.5	32.4	12.3	1.7	66.0	54.5	40.0	41.2	44.0	28.9	41.6	39.7								
21	concrete	N/S canyon	0.293	0.657	0.050	0.032	0.922	0.046	5.2	53.2	44.9	51.1	37.5	7.0	0.6	51.0	45.4	71.7	47.7	61.8	39.5	11.1	1.4	61.4	49.9	41.4	41.7	43.6	35.3	40.8	39.4								
22	concrete	tunnel	0.010	0.990	0.000	0.003	0.997	0.000	0.6	37.6	43.5	38.7	38.7	7.4	1.2	43.1	40.9	39.7	45.6	39.8	39.9	11.6	2.8	48.4	43.8	38.4	41.8	38.5	38.5	40.8	39.5								



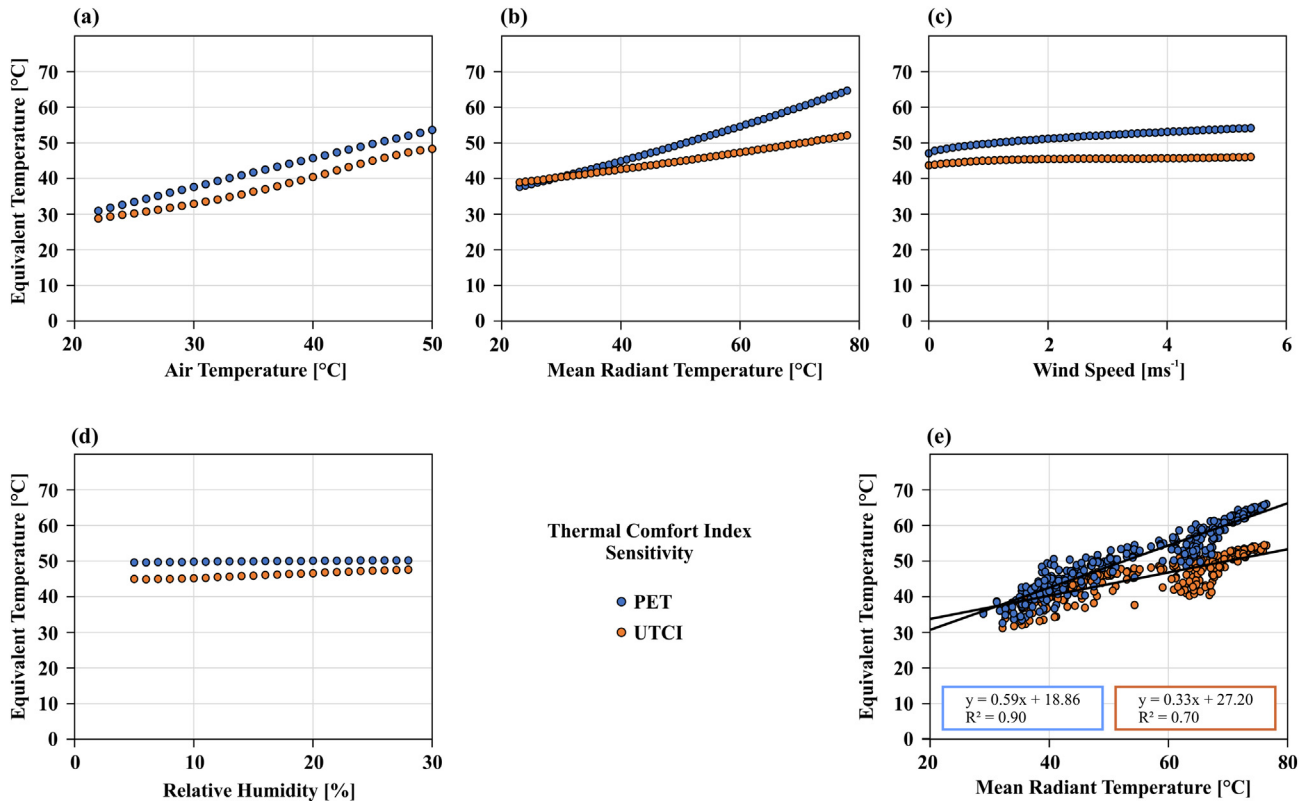


Fig. 5. Sensitivity of *PET* and *UTCI* to each individual meteorological variable composing both stress indices, over their range of variation during the measurement period, holding all other variables constant at their mean values over the measurement period. (a) Air temperature; (b) mean radiant temperature; (c) wind speed; and (d) relative humidity; (e) relationship between observed mean radiant temperature and both stress indices.

their longwave cooling impact over concrete during daytime. Tunnels (locations 2 and 22) receive negligible shortwave radiation and exhibit among the lowest longwave contributions to T_{MRT} ; moreover, the diurnal cycle of T_{MRT} in tunnels is shifted approximately 4 h later than the other sites contributing to the relatively good afternoon *UTCI*/*PET* and relatively poor evening *UTCI*/*PET*.

3.4. Microscale cover and structure controls on directional radiation

Microscale characteristics of the measurement locations modulate the local micrometeorology and resulting contributions to pedestrian thermal exposure (Section 3.2). T_{MRT} dominates the spatio-temporal variation of biometeorological stress indices *PET* and *UTCI*, and the largest components of T_{MRT} are particularly sensitive to shade and secondarily to ground cover (Section 3.3). Therefore, we link T_{MRT} components to basic descriptors of the land cover and radiation geometry of the measurement locations – including 360° view factors of sky (Fig. 8), pervious (vegetated), and impervious surfaces constructed from four orthogonal, horizontally-aimed fish-eye photographs, as well as SVF (Figs. 9–11) – to assess potential microscale design strategies for improved pedestrian thermal comfort in hot, dry conditions.

Least-squared regression analysis incorporating all sites (excluding tunnels) is performed for 12:00 MST, 15:00 MST, and 21:00 MST. During daytime, the degree of solar radiation attenuation plays a dominant role: T_{MRT} and its contribution from shortwave radiation measured by laterally-aimed sensors correlate strongly with SVF at 12:00 MST (Fig. 9a, g), and strong relations persist until 15:00 MST (Fig. 10a, g). For these same times, lateral longwave radiation increases with impervious cover in the lateral field of view, and decreases with corresponding pervious cover (Figs. 9e, f, 10e, f), relations that strengthen further by 21:00 MST and come to dominate T_{MRT} (Fig. 11b, c, e, f). At 21:00 MST, T_{MRT} and the associated lateral longwave contribution are

additionally negatively related to sky fraction within the same lateral view (Fig. 8). These results correspond to the nocturnal surface urban heat island due to increased heat release from impervious surfaces compared to pervious surfaces, and to obstructed sky view by buildings (and trees). Overall, access to solar radiation dominates during the day, and the consistent positive effect of impervious surfaces on longwave contributions to T_{MRT} suggests a microscale surface urban heat island exists throughout the afternoon and in the evening (i.e., impervious surfaces are warmer than pervious surfaces).

Trees count toward the 360° pervious fraction but behave differently compared to grass and other low vegetation in terms of microscale radiation exchange because they intercept shortwave radiation (i.e., provide shade) and impact longwave radiation exchange via reduction of the SVF. Therefore, we assess sites situated at some distance from trees or solar canopies (locations 1, 4, 5, 7, 10–12, 14, 16, 19–21) separately from sites located directly under trees (3, 6, 8, 9, 15, 17, 18). At noon and mid-afternoon, T_{MRT} and its lateral components at sites without trees or artificial shade are only weakly related to SVF. Instead, lateral longwave contributions vary with fractions of pervious vs. impervious in the lateral view of the sensors (Figs. 9e, f, 10e, f); in other words, ground cover, not SVF, dominates daytime T_{MRT} in locations without direct shade. Strong radiative warming related to impervious fraction and radiative cooling related to pervious fraction persist into the evening, and SVF becomes important during this cooling portion of the diurnal cycle (Fig. 11a–f). At locations under trees, conversely, SVF dominates during the day, with larger SVF increasing T_{MRT} via enhanced lateral (and downward) shortwave, and to a lesser degree, lateral longwave (Figs. 9a, g, 10a, d, g). SVF in this case is an inverse proxy for shade; furthermore, smaller daytime SVF (i.e., more direct shade from trees) also leads to cooler ground surface temperatures and smaller longwave contributions to T_{MRT} . Notably, increased impervious fraction in the lateral view enhances lateral longwave and T_{MRT} even under tree cover, and pervious fraction has the opposite effect, particularly at 21:00 MST

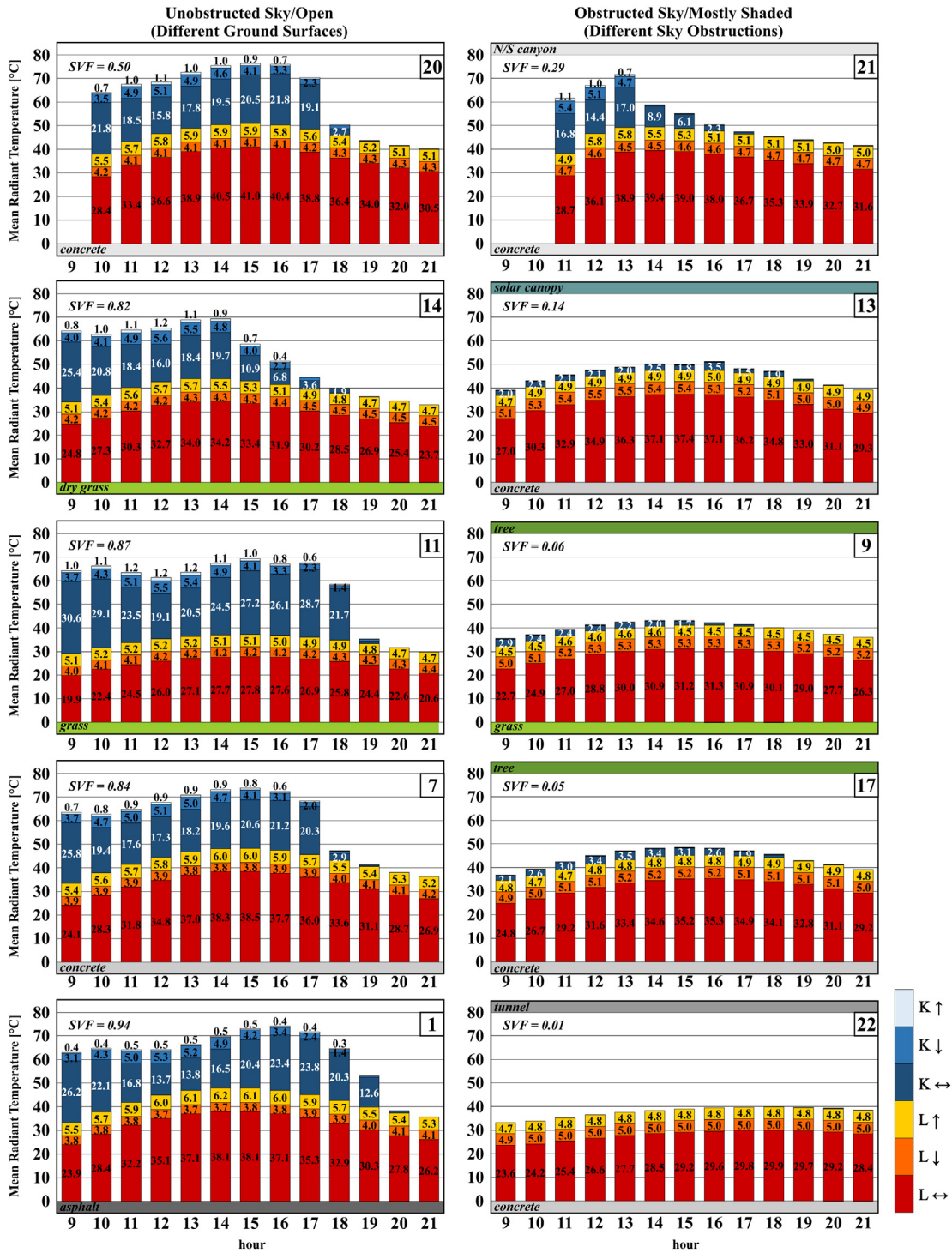


Fig. 6. Decomposed mean radiant temperature (T_{MRT}) for select sites, illustrating the contributions of directional longwave (L) and shortwave (K) radiation to the mean radiant temperature profile (for other locations see Fig. 7).

(Fig. 11b, c, e, f), meaning that impervious surfaces are warmer relative to grass even in locations with substantial tree shade and remain comparatively warm into the evening at these locations. This effect is about half as large as it is in locations without trees.

From the regression slopes in Figs. 9–11 the magnitudes of impervious, pervious and sky view fraction impacts on T_{MRT} can be derived for extreme heat conditions in Phoenix (note, however, that these relations are not independent). As expected, sky obstruction (shading) from trees is demonstrably impactful on T_{MRT} and its lateral shortwave component, decreasing T_{MRT} by 4 °C per tenth of the sky view obstructed, on average

(see slopes in Figs. 9a and 10a). This effect is larger as the afternoon progresses (15:00 MST vs. 12:00 MST), and trees reduce lateral longwave contributions to T_{MRT} by about 1 °C per tenth of sky view obstructed as well by mid-afternoon, by keeping ground and vertical surfaces cooler (Fig. 10d). At this time of day, in other words, about three quarters of the T_{MRT} reductions from tree shade derive directly from shading, and approximately one quarter arise indirectly from reduced longwave emission from the cooler, shaded ground.

Irrespective of shade from trees, an increase of pervious fraction (and corresponding decrease of impervious fraction) that is equivalent

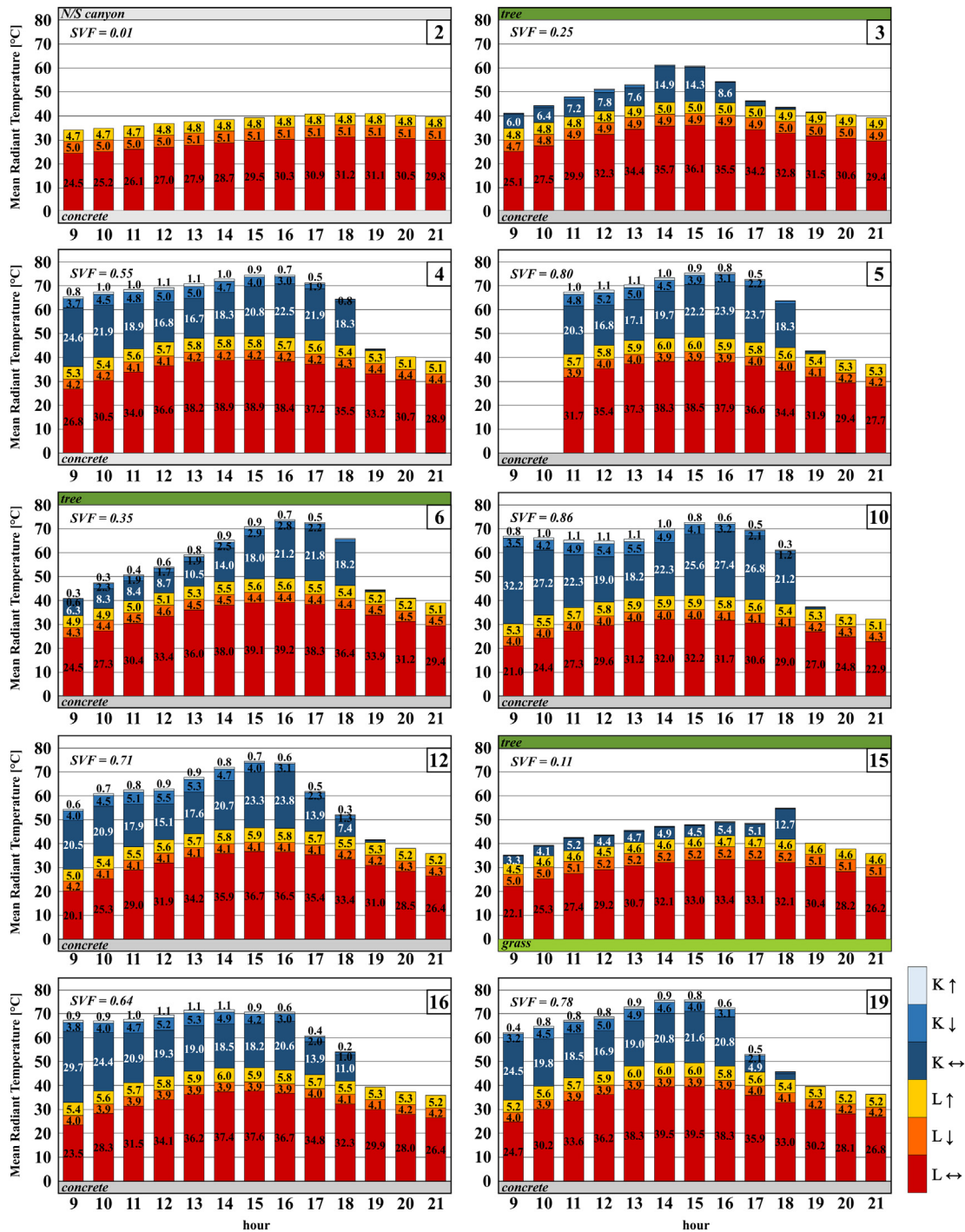


Fig. 7. Decomposed mean radiant temperature for select sites, illustrating the contributions of directional longwave (L) and shortwave (K) radiation to the mean radiant temperature profile (for other locations see Fig. 6).

to 10% of the field of view of the four lateral sensors (360° field of view) yields a ca.1 °C reduction of T_{MRT} at 12:00 MST for these conditions. This cooling increases by approximately 30% by mid-afternoon and is non-negligible even at sites with substantial shading (e.g., from trees). By evening, impervious view fraction clearly increases T_{MRT} (ca. 1.4 °C increase of T_{MRT} per 10% of lateral view factor for sites without trees), while pervious view fraction and SVF decrease T_{MRT} by a similar magnitude; sites with sky obstruction by trees show muted versions of the same effects.

In summary, T_{MRT} at sites without sky obstruction from trees or artificial canopies is principally modulated by its lateral (and upward)

longwave contributions during the afternoon and evening, and by the relation of these longwave contributions to pervious, impervious and sky fractions. At these sites, T_{MRT} can most effectively be reduced by addition of shade, and secondarily by replacement of impervious with pervious surfaces. In addition to replacement of impervious with pervious cover, evening T_{MRT} can effectively be reduced by increasing exposure to the sky, suggesting that devices designed to block shortwave radiation but facilitate longwave exchange with the cool sky would be optimal solutions. Tree planting represents a tradeoff for these hot, dry conditions: trees yield large daytime T_{MRT} reductions, but demonstrate a smaller, but clear, radiant warming effect at night. At sites that already

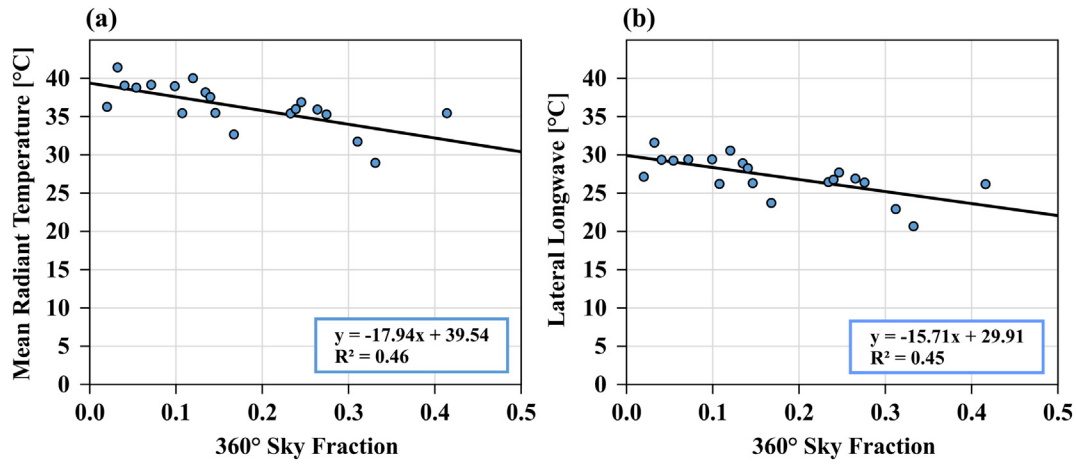


Fig. 8. Relationship between 360° sky fraction and mean radiant temperature (a), and lateral longwave contribution to T_{MRT} (b), at 21:00 MST.

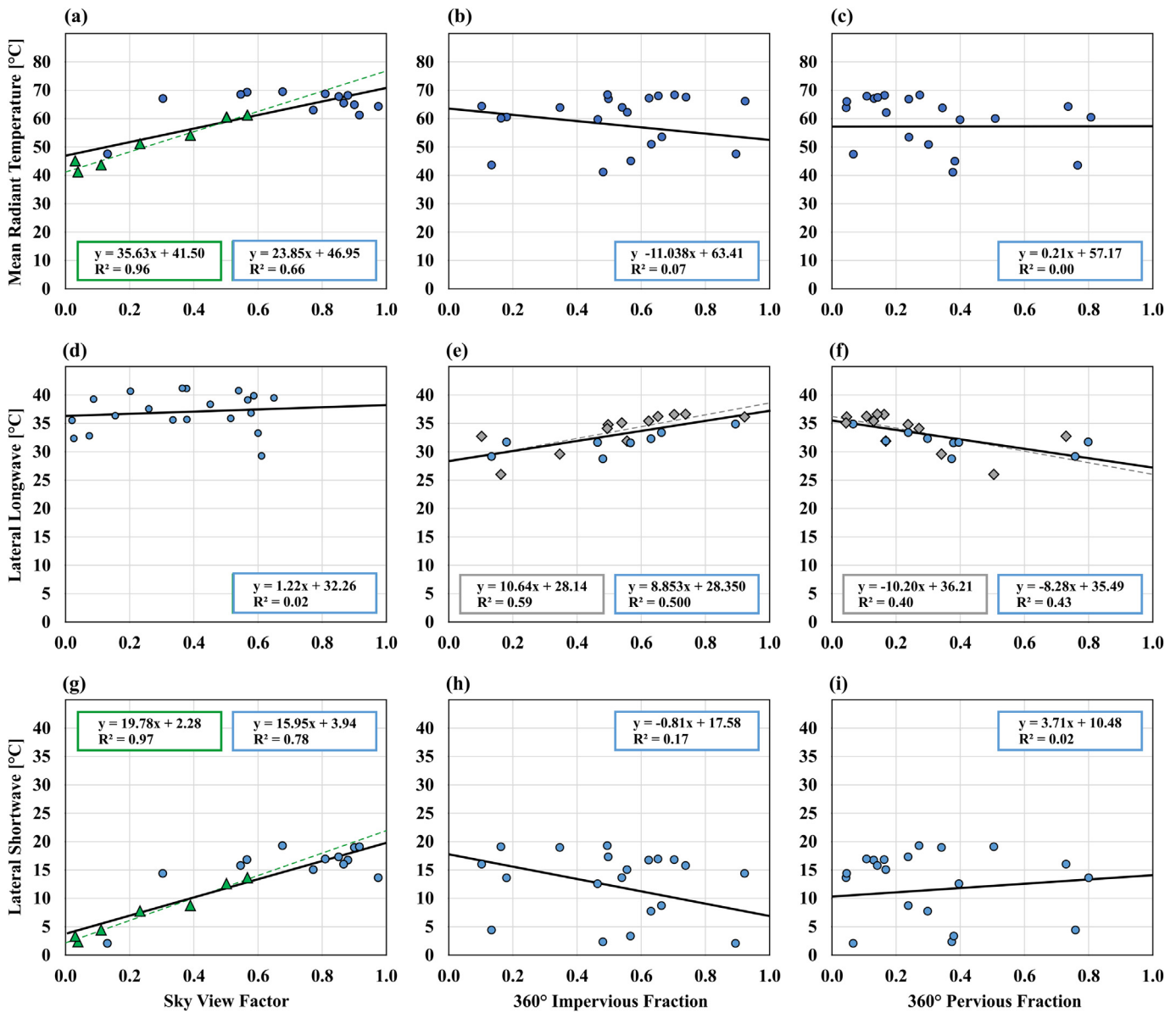


Fig. 9. Scatter plots and least-square regression of T_{MRT} and associated contributions from lateral longwave and lateral shortwave against characterizations of the microscale three-dimensional environment of relevance to radiation exchange (12:00 MST). Blue circles denote all sampled locations; green triangles are a subset of locations that are shaded by trees; grey diamonds are a subset of locations that are not shaded by trees or tunnels.

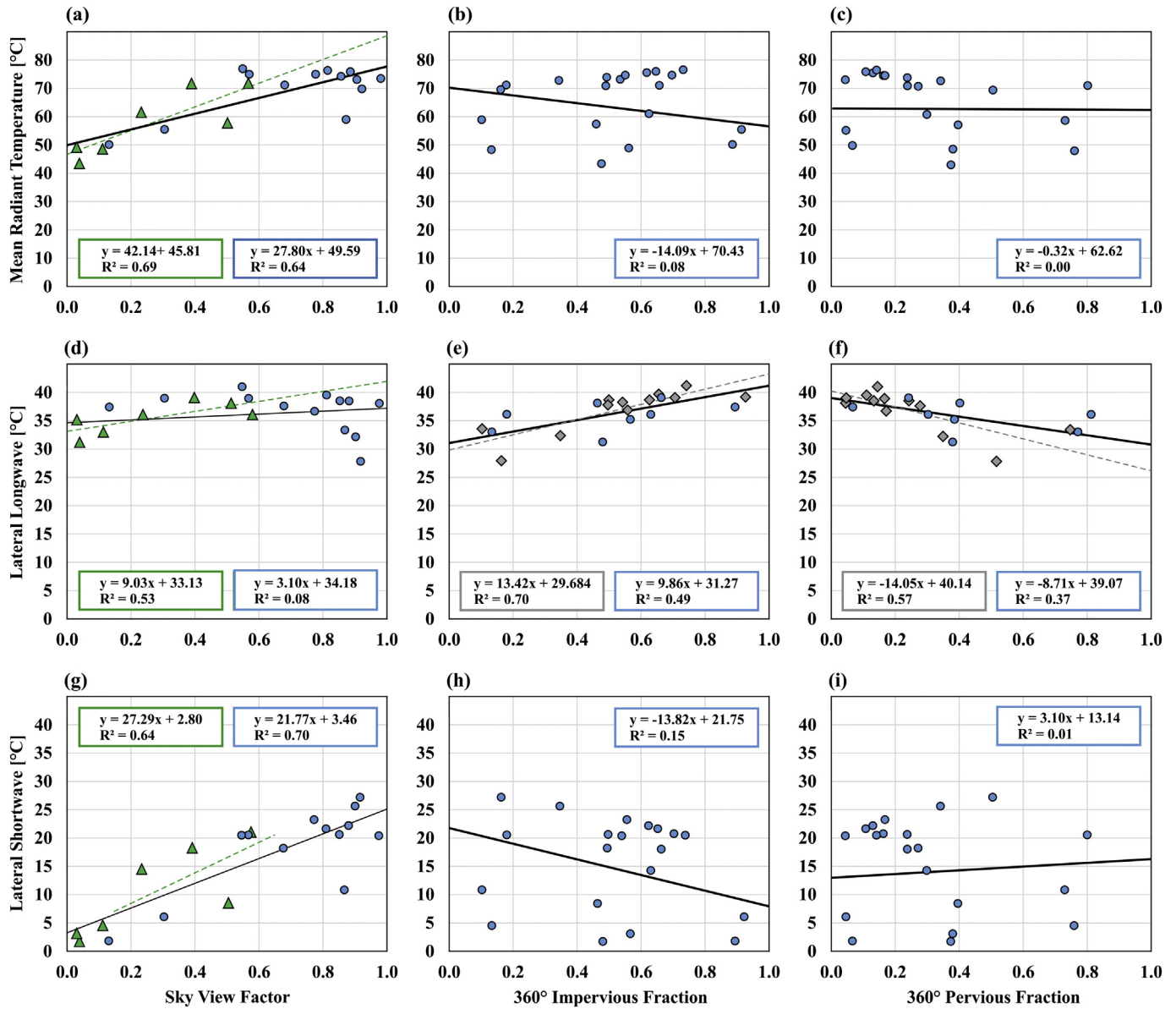


Fig. 10. Scatter plots and least-square regression of T_{MRT} and associated contributions from lateral longwave and lateral shortwave against characterizations of the microscale three-dimensional environment of relevance to radiation exchange (15:00 MST). Symbols are as in Fig. 9.

have substantial tree cover, both shortwave and longwave contributions play a role in the spatial variability of T_{MRT} , and SVF is important. Thus, increasing tree coverage and/or density reduces daytime T_{MRT} and increases evening (and nighttime) T_{MRT} ; for most conditions, this tradeoff is advantageous, except for extremely hot days. Replacement of impervious ground surfaces under trees with pervious cover can contribute to both daytime and nighttime reductions of T_{MRT} and represents an ideal adaptation option for extreme heat during both daytime and evening periods.

4. Discussion

Spatial variation of pedestrian thermal exposure is dominated by T_{MRT} for the hot, dry, low wind conditions investigated in this contribution. The subsequent discussion therefore focuses on T_{MRT} . We presented 3-dimensional shortwave and longwave radiant flux contributions to the mean radiant temperature under the most extreme heat conditions that have been recorded with the six-directional net radiometer setup. On a dry June day with record-breaking temperatures in Tempe, AZ, T_a peaked locally at 48.5 °C with a maximum T_{MRT} of

76.4 °C at 15:00 MST in an east-west building canyon. Comparative studies in more temperate climates observed maxima of $T_a = 35.0$ °C and $T_{MRT} = 66$ °C in Freiburg, Germany (Ali-Toudert and Mayer, 2007) and $T_a = 31.0$ °C and $T_{MRT} = 65$ °C in Szeged, Hungary (Kántor et al., 2016). In agreement with other observational studies, T_{MRT} was most variable between shaded and sun-exposed sites (max $\Delta T_{MRT} \approx 40$ °C), followed by T_s (max $\Delta T_s \approx 30$ °C) and T_a (max $\Delta T_a = 4.4$ °C), highlighting the importance of the radiant flux densities for characterization of spatial variability of human thermal exposure and comfort.

To most accurately capture thermal conditions during the transects, we time-detrended the observations and discarded records that were subject to sensor lag or human interference. As the Hukseflux NR-01 radiometers have a field-of-view of 150°, the orientation of the sensors matters. For example, the shortwave radiation received by the east, west, and south facing pyranometers is slightly underestimated between 1220 and 1250 MST when the sun altitude is above 75°. We used a pre-defined, consistent cart orientation at each transect stop that aligned with one of the four cardinal directions to minimize errors caused by orientation inconsistencies. The field-of-view limitation of the lateral sensors affected six observations during the noon transect

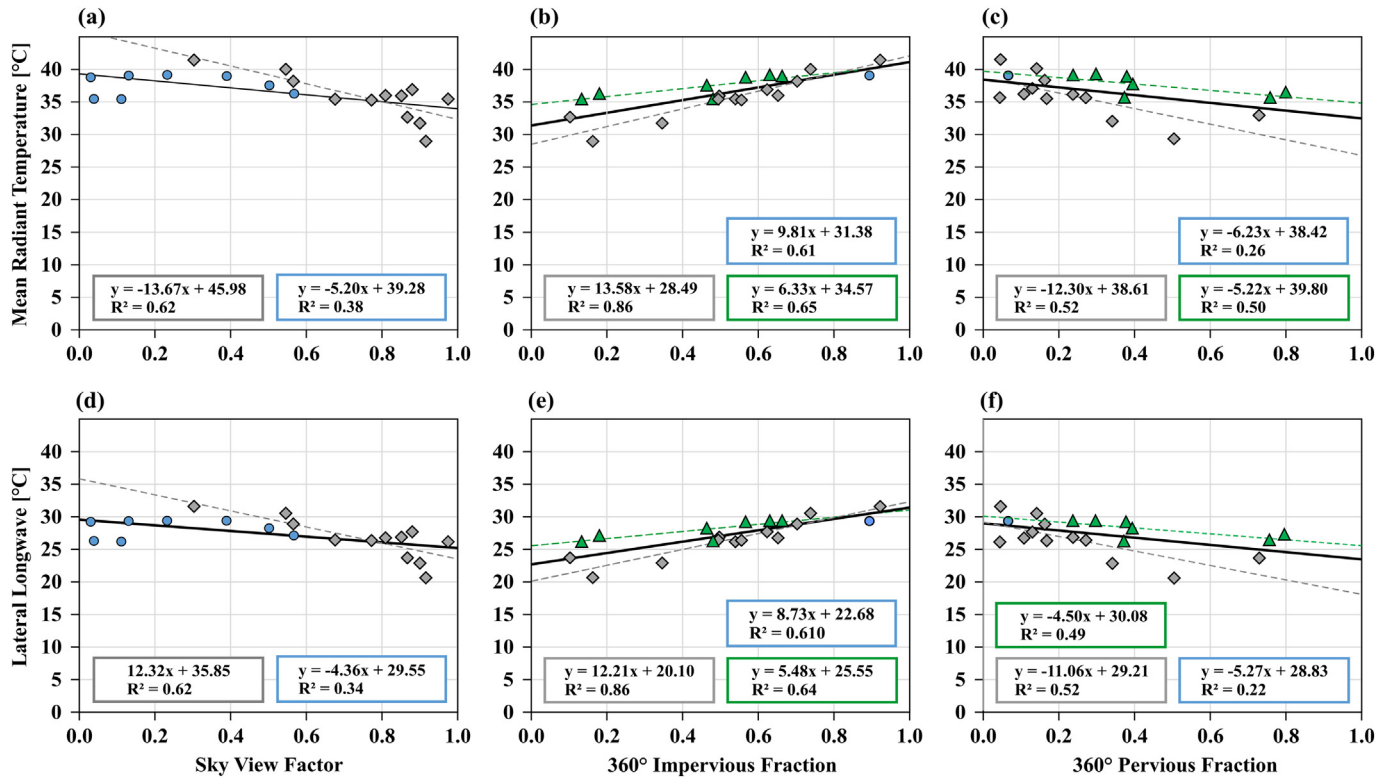


Fig. 11. Scatter plots and least-square regression of T_{MRT} and associated contributions from lateral longwave and lateral shortwave against characterizations of the microscale three-dimensional environment of relevance to radiation exchange (21:00 MST). Symbols are as in Fig. 9.

(locations 12, 14, 16, 19–21) and is noticeable in Figs. 6 and 7 but did not significantly affect the results. Small measurement errors are potentially introduced through the cart itself, which is in the field of view of the downward and lateral facing radiometers. *MaRTy*'s design carefully balances degree of self-obstruction, maneuverability, and radiometer offset from the center.

To describe the human energy balance under extreme heat conditions more holistically, we calculated the thermal comfort indices *UTCI* and *PET* for a 35-year old 1.7-m standing male. *UTCI* and *PET* peaked at 54.5 °C and 66.0 °C, respectively, in an E-W building canyon with light colored concrete (location 20). Results are consistent with findings from Lee and Mayer (2018) who showed in a modeling study that increased albedo of building walls in E-W canyons raises T_{MRT} and *PET*. While high albedo surfaces exhibit lower T_s during the day, they increase the amount of reflected shortwave radiation, which reduces outdoor thermal comfort (Erell et al., 2014) and can also increase building internal heat loading (Yaghoobian et al., 2010).

In a sensitivity analysis of *UTCI* and *PET* to meteorological input variables, both indices were more sensitive to a change in T_a than T_{MRT} . Yet, since T_{MRT} observations were more variable than the corresponding indices, T_{MRT} was a better predictor of the spatio-temporal variability of pedestrian thermal experience. This is in line with Lee et al. (2014) who found T_{MRT} to be a better predictor for *PET* than T_a . In a comfort index comparison study, Blazejczyk et al. (2012) also found that T_a is relatively well correlated with *UTCI*, while weaker relationships were discovered for T_{MRT} .

UTCI and *PET*, despite considering the complete heat budget of the human body, have limitations. Both indices have not been validated for the extreme conditions present in this study. $T_a = 48.5$ °C is at the upper limit of the recommended range for *UTCI*, and the parameterizations might not be valid under extreme heat, for example with respect to clothing. Insulation is modeled as a function of ambient temperature based on observed seasonal clothing adaptation habits of Europeans (Havenith et al., 2012), which may not apply to an Arizona population

that moves between air-conditioned spaces. In addition, the scales for *UTCI* and *PET* have not been calibrated for extreme hot and dry environments using survey data. In temperate climates, *PET* > 35 °C suggests “strong heat stress” and *PET* > 41 °C means “extreme heat stress”, but these grades of physiological stress will be different in hot, dry environments. Unfortunately, a calibrated scale for *PET* and *UTCI* does not exist for Phoenix. We hypothesize that the thresholds will be shifted upwards, i.e. extreme heat stress in Phoenix starts at higher temperatures. Using the scale for temperate climates yields “extreme heat stress” for all locations and times of day except at the two tunnel locations before noon. Ultimately, no conclusions can be made about how the indices translate into thermal sensation votes, although it is very likely that most of our observations fall into the “extreme heat stress” category.

We investigated the microscale controls on T_{MRT} through assessment of the weighted directional shortwave and longwave radiative flux density contributions as they are absorbed by the human body. Incident lateral longwave radiation was found to be the dominant factor in the radiation budget, while incident lateral shortwave radiation was most variable across all T_{MRT} profiles, reflecting the various shade conditions and SVFs. Although measured longwave flux densities are smaller than shortwave flux densities, the latter derive principally from the direction associated with the solar azimuth and zenith angles—that is, only two of the four lateral shortwave sensors receive direct shortwave radiation. Similarly, only one side of the standing human body is illuminated by direct shortwave radiation, whereas all sides of the body (and all sensors) receive longwave radiation. This explains why T_{MRT} (and therefore overall pedestrian thermal exposure, for these meteorological conditions) is typically dominated by the longwave radiation flux and generally confirms findings by Ali-Toudert and Mayer (2007) and Lee et al. (2014) in Freiburg, Germany. However, notable exceptions in Tempe are sunlit locations in the morning, when longwave contributions to T_{MRT} are modest because surface temperatures have yet to approach the diurnal maximum, and larger solar zenith angles lead to

substantial shortwave flux densities on the lateral sensors (vertical surfaces of a standing person). Transect stops on exposed grass, asphalt, and concrete surfaces exhibited higher absorbed shortwave than longwave flux densities at 09:00 MST.

Further examination of the directional flux densities showed that the largest contributors to T_{MRT} are particularly sensitive to shade (with peak discomfort in the afternoon at sun-exposed locations), and secondarily to ground cover. Lindberg et al. (2016) conducted integral six-directional measurements at King's College, London and found that the influence of ground cover materials on T_{MRT} was small compared to the impact of shade. Our results suggest that during extreme heat, the ground surface type has a small but non-negligible impact on T_{MRT} , even in the shade. Grass with sufficient irrigation reduced T_{MRT} and improved comfort both day and night relative to concrete, even under dense tree cover. This is possibly due to a micro-oasis effect which leads to reduced ground surface temperature with grass cover relative to impervious surface covers, and in turn lowers lateral and upwelling longwave fluxes. Impervious surfaces were warmer than pervious surfaces at all measurement times and are significant predictors of lateral and upward longwave and therefore T_{MRT} . Increased lateral longwave contributions from impervious surfaces indicates that a microscale surface urban heat island exists throughout the afternoon and evening (i.e., impervious surfaces are always warmer than pervious surfaces).

To determine the impact of urban form and composition on the radiation budget, we calculated view factors for sky (SVF), buildings (BVF), and vegetation (VVF, includes trees, shrubs, and grass). Afternoon T_{MRT} was best explained by the traditional upper hemisphere SVF ($R^2 = 0.71$) and sun duration ($R^2 = 0.76$), further underlining that shortwave radiation is the driving factor for T_{MRT} variation between sites. On average, T_{MRT} decreased by 4 °C per tenth of the sky view obstructed. Holst and Mayer (2011) investigated the impact of street design parameters on human biometeorological variables in Freiburg, Germany and found a relationship of similar magnitude between SVF_{90-270} (the SVF of the lower half of the upper hemisphere), and T_{MRT} ($R^2 = 0.764$). They also found that street tree coverage is important for explanation of T_{MRT} variation ($R^2 = 0.763$).

Tree planting constitutes a tradeoff for extremely hot, dry conditions. During the day, we observed large daytime T_{MRT} reductions under trees (up to 33.4 °C), but measurements after sunset demonstrated a smaller, yet clear warming effect at night of up to 5 °C. This warming effect can likely be attributed to the tree canopy emitting more longwave than the cold sky, and has been documented in previous observational studies (Golden et al., 2007; Coutts et al., 2016; Middel et al., 2016). While the value of tree planting for reduction of urban heat islands is commonly extolled, our results suggest that biometeorological stress may be exacerbated by urban trees at night, when heat islands are typically maximized. Additional six-directional longwave and shortwave radiation measurements across the diurnal cycle in range of cities would help assess the impacts of urban trees across the diurnal cycle for a range of conditions. Irrespective of the urban heat island, our results suggest that urban trees have an important role in biometeorological stress reduction during daytime via provision of shade.

View factors in this study were calculated based on manually classified fisheye photos. Recent developments in artificial intelligence offer the unprecedented opportunity to use algorithms that automatically detect urban surface types using machine learning, as demonstrated by Middel et al. (2019).

5. Conclusions

All biometeorologically-relevant variables, including six-direction longwave and shortwave radiation, were measured on a record-breaking extreme heat day in Tempe, Arizona, using a unique, mobile biometeorological instrument platform (MaRTy). Measurements were conducted hourly for 12 h during the hottest half of the day, and at 22 distinct locations in an Open Midrise neighborhood, sampling a range

of sky cover (building heights, tree density, photovoltaic panels) and ground cover (asphalt, concrete, dry and irrigated grass). Peak measured air temperature (T_a), surface temperature (T_s), mean radiant temperature (T_{MRT}) were 48.5 °C, 65.8 °C, and 76.4 °C, respectively.

5.1. Summary of findings

Primary conclusions with regards to pedestrian thermal exposure and its modulation via urban design for these very hot and dry conditions, near the summer solstice, are as follows.

Overall pedestrian thermal exposure (PET and $UTCI$):

- PET and $UTCI$ thermal exposure indices peak during the afternoon between 16:00 and 17:00 MST at 66.0 °C and 54.5 °C, respectively, in an E-W oriented canyon with concrete floors and walls;
- Afternoon thermal exposure is least in locations with grass and with trees providing shade, and in tunnels under buildings; evening thermal exposure is least in open grassy areas;
- Tree cover yields large daytime PET and $UTCI$ reductions, but small evening increases of 1–2 °C;
- Grass reduces thermal exposure during afternoon and evening relative to engineered surfaces – even under dense tree cover, probably due to a micro-oasis effect;
- PET and $UTCI$ are driven principally by T_a and T_{MRT} (i.e., T_s and solar radiation) for these conditions. Both indices are more sensitive to T_a than T_{MRT} per degree K variation. However, T_{MRT} is an order of magnitude more variable spatially (and also more variable temporally) compared to T_a , rendering T_{MRT} a better predictor of the spatio-temporal variation of thermal exposure in the neighborhood.

Radiant pedestrian thermal exposure (T_{MRT}):

- Except for morning hours, longwave radiation fluxes contribute more to T_{MRT} magnitude than shortwave radiation fluxes, even in direct sunlight; however, shortwave radiation fluxes exhibit greater spatial (and temporal) variation;
- Lateral radiant exposure, particularly lateral longwave exposure, contributes the majority of T_{MRT} magnitude at all times and sites, suggesting that cool vertically-oriented surfaces adjacent to pedestrian walkways may effectively reduce pedestrian thermal exposure;
- Trees increase T_{MRT} by up to 5 °C (3 °C) in the evening when situated above grass (concrete); trees exert a daytime longwave radiant increase above grass, but daytime longwave radiant cooling over concrete.
- Because photovoltaic panels emit more downward longwave toward pedestrians, daytime shade from a 7.5 m elevated solar photovoltaic canopy yields a T_{MRT} reduction that is 3 °C smaller than daytime shade from a tree canopy with the same SVF;
- In the absence of shade, irrigated grass lowers T_{MRT} by >10 °C during afternoon relative to asphalt or concrete, and by about half as much after sunset – dry grass provides about half as much T_{MRT} reduction as irrigated grass at both times of day;
- Even under near-complete shade from trees, irrigated grass provides a 3–4 °C reduction of T_{MRT} relative to concrete during both afternoon and evening.

Microscale design for cool pedestrian spaces:

- Shade (reduction of shortwave from increased sky cover) is the most important consideration for daytime T_{MRT} reduction – T_{MRT} is reduced by about 4 °C per 0.1 SVF decrease due to tree cover;
- Replacement of impervious ground cover (asphalt, concrete) with pervious cover (grass) reduces T_{MRT} at all times of day, by approximately 1.0–1.5 °C per tenth of the local land cover converted from

impervious to pervious; along with increased SVF, this is the most important consideration to lower T_{MRT} after sunset;

- At sites with little or no direct shade from trees or buildings, ground cover controls T_{MRT} during daytime; SVF and ground cover control T_{MRT} in the evening;
- Under trees, SVF (i.e., density and position of tree cover) correlates positively with daytime T_{MRT} via both shortwave and longwave radiation – about 75% of the T_{MRT} reduction as SVF is reduced by tree cover is attributable to direct reduction of shortwave incident on the pedestrian, and the remaining 25% is attributable to reduction of longwave radiation from the cooler ground.
- Trees have a greater radiant cooling impact, particularly during daytime, when planted over concrete compared to grass

5.2. Context and significance

A recent study concluded that reductions of air temperature from ‘full adaptation’, that is, uniform, high-intensity and joint implementation of street trees, green and cool (reflective) roofs, was insufficient to offset end-of-21st century climate change warming in all U.S. cities during nighttime, as well as during daytime for the RCP 8.5 greenhouse gas emissions scenario (Krayerhoff et al., 2018). These results suggest that, barring substantive climate change mitigation, urban heat exposure is likely to increase dramatically, even with extensive urban heat adaptation. Outdoor pedestrian thermal exposure represents one component of overall human heat exposure in cities, which also includes exposure in vehicles and indoors (relating to building design and indoor temperature regulation). Outdoor thermal comfort depends on several factors, including exposure to wind, humidity and radiant loads, in addition to air temperature. Therefore, while urban air temperatures may increase under climate change irrespective of large-scale adaptation, strategies that target other biometeorologically-relevant variables may provide additional opportunities for cooling sidewalks and other pedestrian corridors and may have the potential to fully offset climate change warming from a biometeorological perspective.

Wind and radiant loads on a pedestrian exhibit large spatiotemporal variation at microscales and provide opportunity for microscale adaptation strategies. Air temperature and humidity, conversely, tend to be more homogenous at these scales, varying more substantively at local scales (100 m – 5 km) in cities (e.g., Stewart et al., 2014). Our results suggest, for the hot dry climates common during summer in many areas of the U.S. Southwest (albeit for temperatures that are currently rare, but may become increasingly less so), several design options that decrease radiant loading on pedestrians.

Our results demonstrate that shade is the most important design tool for outdoor pedestrian spaces during very hot, low wind conditions in these dry climates. Secondly, replacement of impervious materials with pervious cover, especially when irrigated, provides radiant cooling to pedestrians throughout the afternoon and evening, even when shaded, whereas trees slightly worsen thermal conditions by mid-evening. There is evidence that trees can increase nocturnal air temperature (Gillner et al., 2015), and our results suggest that they also increase nighttime longwave radiation exposure of pedestrians. While trees have smaller longwave radiant warming impacts when planted over concrete (e.g. sidewalks) compared to grass (e.g., a park), they effectively reduce pedestrian radiant exposure during daytime clear sky conditions above all ground covers assessed here, due to the large shortwave reductions they produce. More rigorous assessment of day-night thermal comfort tradeoffs of urban tree planting across a range of climates, ground covers, and neighborhood configurations would be helpful.

Our results also suggest that cooling vertical surfaces adjacent to pedestrian walkways (e.g., the lower portions of building walls located adjacent to sidewalks) may have substantive benefits for pedestrians for these conditions. This could be achieved, for example, by greening or

irrigating lower building walls, or increasing their thermal admittance (which, conversely, would increase evening and nocturnal air temperatures). Trees, grass, and irrigation more generally often depend on availability of water resources, which are uncertain in many hot, dry regions under future climate scenarios. In this light, some combination of grass under drought-tolerant trees, photovoltaic panels or other shading devices (which are ideally retracted during evening and night), and high thermal admittance building wall bases, deployed in key pedestrian areas, may substantively reduce thermal exposure and associated ill effects for many pedestrians while minimizing water use.

CRedit authorship contribution statement

Ariane Middel: Conceptualization, Formal analysis, Methodology, Writing - original draft, Writing - review & editing, Funding acquisition. **E. Scott Krayerhoff:** Conceptualization, Formal analysis, Methodology, Writing - original draft, Writing - review & editing.

Declaration of Competing Interest

The authors declare no competing interests. Funding sources had no direct involvement in the study.

Acknowledgements

This research was sponsored by University of Kaiserslautern, grant “Microclimate Data Collection, Analysis, and Visualization”, the US National Science Foundation (NSF) under grants SES-1520803, CBET-1444758 and CMMI-1635490 (Urban Water Innovation Network), and a Natural Sciences and Engineering Research Council of Canada (NSERC) Discovery Grant. Any opinions, findings, and conclusions or recommendations expressed in this material are those of the authors and do not necessarily reflect the views of the sponsoring organizations. The authors thank Jennifer Vanos and David Sailor for assisting with design of the *MaRTy* platform.

References

- ADHS, 2018. Extreme weather & public health. <https://www.azdhs.gov/preparedness/epidemiology-disease-control/extreme-weather/heat-safety/index.php#heat-illness>.
- Ali-Toudert, F., Mayer, H., 2007. Thermal comfort in an east-west oriented street canyon in Freiburg (Germany) under hot summer conditions. *Theor. Appl. Climatol.* 87, 223–237. <https://doi.org/10.1007/s00704-005-0194-4>.
- Argüeso, D., Evans, J.P., Fita, L., Bormann, K.J., 2014. Temperature response to future urbanization and climate change. *Clim. Dyn.* 42 (7–8), 2183–2199.
- Basu, R., 2009. High ambient temperature and mortality: a review of epidemiologic studies from 2001 to 2008. *Environ. Heal. A Glob. Access Sci. Source* 8, 40. <https://doi.org/10.1186/1476-069X-8-40>.
- Bierwagen, B.G., Theobald, D.M., Pyke, C.R., Choate, A., Groth, P., Thomas, J.V., Morefield, P., 2010. National housing and impervious surface scenarios for integrated climate impact assessments. *Proc. Natl. Acad. Sci.* 107, 20887–20892. <https://doi.org/10.1073/pnas.1002096107>.
- Blazejczyk, K., Epstein, Y., Jendritzky, G., Staiger, H., Tinz, B., 2012. Comparison of UTCI to selected thermal indices. *Int. J. Biometeorol.* 56, 515–535. <https://doi.org/10.1007/s00484-011-0453-2>.
- Bröde, P., Fiala, D., Blazejczyk, K., Holmér, I., Jendritzky, G., Kampmann, B., Tinz, B., Havenith, G., 2012. Deriving the operational procedure for the Universal Thermal Climate Index (UTCI). *Int. J. Biometeorol.* 56, 481–494. <https://doi.org/10.1007/s00484-011-0454-1>.
- Bucchignani, E., Mercogliano, P., Panitz, H.J., Montesarchio, M., 2018. Climate change projections for the Middle East–North Africa domain with COSMO-CLM at different spatial resolutions. *Adv. Clim. Chang. Res.* 9 (1), 66–80.
- Coutts, A.M., White, E.C., Tapper, N.J., Beringer, J., Livesley, S.J., 2016. Temperature and human thermal comfort effects of street trees across three contrasting street canyon environments. *Theor. Appl. Climatol.* 124, 55–68. <https://doi.org/10.1007/s00704-015-1409-y>.
- Erell, E., Pearlmutter, D., Boneh, D., Kutiel, P.B., 2014. Effect of high-albedo materials on pedestrian heat stress in urban street canyons. *Urban Clim* 10, 367–386. <https://doi.org/10.1016/j.uclim.2013.10.005>.
- Georgescu, M., Morefield, P.E., Bierwagen, B.G., Weaver, C.P., 2014. Urban adaptation can roll back warming of emerging megapolitan regions. *Proc. Natl. Acad. Sci.* 111 (8), 2909–2914.
- Gillner, S., Vogt, J., Tharang, A., Dettmann, S., Roloff, A., 2015. Role of street trees in mitigating effects of heat and drought at highly sealed urban sites. *Landsc. Urban Plan.* 143, 33–42.

- Golden, J.S., Carlson, J., Kaloush, K.E., Phelan, P., 2007. A comparative study of the thermal and radiative impacts of photovoltaic canopies on pavement surface temperatures. *Sol. Energy* 81 (7), 872–883.
- Gosling, S.N., Lowe, J.A., McGregor, G.R., Pelling, M., Malamud, B.D., 2009. Associations between elevated atmospheric temperature and human mortality: a critical review of the literature. *Clim. Chang.* 92, 299–341. <https://doi.org/10.1007/s10584-008-9441-x>.
- Hüb, K., Ruddell, B.L., Middel, A., 2015. Sensor lag correction for mobile urban microclimate measurements. *Urban Clim* 14, 622–635. <https://doi.org/10.1016/j.uclim.2015.10.003>.
- Harlan, S.L., Brazel, A.J., Prasad, L., Stefanov, W.L., Larsen, L., 2006. Neighborhood microclimates and vulnerability to heat stress. *Soc. Sci. Med.* 63, 2847–2863. <https://doi.org/10.1016/j.socscimed.2006.07.030>.
- Havenith, G., Fiala, D., Blazejczyk, K., Richards, M., Bröde, P., Holmér, I., Rintamaki, H., Benschabat, Y., Jendritzky, G., 2012. The UTCI-clothing model. *Int. J. Biometeorol.* 56, 461–470. <https://doi.org/10.1007/s00484-011-0451-4>.
- Holst, J., Mayer, H., 2011. Impacts of street design parameters on human-biometeorological variables. *Meteorol. Zeitschrift* 20, 541–552. <https://doi.org/10.1127/0941-2948/2011/0254>.
- Hondula, D.M., Balling, R.C., Andrade, R., Scott Krayenhoff, E., Middel, A., Urban, A., Georgescu, M., Sailor, D.J., 2017. Biometeorology for cities. *Int. J. Biometeorol.* 61, 59–69. <https://doi.org/10.1007/s00484-017-1412-3>.
- Hondula, D.M., Sabo, J., Quay, R., Chester, M., Georgescu, M., Grimm, N., Harlan, S., Middel, A., Rittmann, B., Ruddell, B., White, D., 2019. Southwest cities are testbeds for urban resilience to a warming world. *Front. Ecol. Environ.* 17, 79–80. <https://doi.org/10.1002/fee.2005>.
- Höppe, P., 1992. A new procedure to determine the mean radiant temperature outdoors. *Wetter und Leb* 44, 147–151.
- Höppe, P., 1999. The physiological equivalent temperature - a universal index for the biometeorological assessment of the thermal environment. *Int. J. Biometeorol.* 43, 71–75. <https://doi.org/10.1007/s004840050118>.
- Intergovernmental Panel on Climate Change, 2014. Climate change 2014 synthesis report - IPCC, climate change 2014: synthesis report. Contribution of Working Groups I, II and III to the Fifth Assessment Report of the Intergovernmental Panel on Climate Change <https://doi.org/10.1017/CBO9781107415324>.
- ISO, 1998. ISO 7726, Ergonomics of the Thermal Environment, Instruments for Measuring Physical Quantities. *Int. Stand. Organ.* Geneva (doi:ISO 7726:1998 (E)).
- Jendritzky, G., de Dear, R., Havenith, G., 2012. UTCI—why another thermal index? *Int. J. Biometeorol.* 56, 421–428. <https://doi.org/10.1007/s00484-011-0513-7>.
- Johansson, E., Thorsson, S., Emmanuel, R., Krüger, E., 2014. Instruments and methods in outdoor thermal comfort studies – the need for standardization. *Urban Clim* 10, 346–366. <https://doi.org/10.1016/j.uclim.2013.12.002>.
- Kántor, N., Kovács, A., Takács, Á., 2016. Small-scale human-biometeorological impacts of shading by a large tree. *Open Geosci* 8, 231–245. <https://doi.org/10.1515/geo-2016-0021>.
- Kántor, N., Chen, L., Gál, C.V., 2018. Human-biometeorological significance of shading in urban public spaces—summer time measurements in Pécs, Hungary. *Landsc. Urban Plan.* 170, 241–255. <https://doi.org/10.1016/j.landurbplan.2017.09.030>.
- Krayenhoff, E.S., Christen, A., Martilli, A., Oke, T.R., 2014. A multi-layer radiation model for urban neighbourhoods with trees. *Boundary-layer meteorol* 151, 139–178. <https://doi.org/10.1007/s10546-013-9883-1>.
- Krayenhoff, E.S., Moustau, M., Broadbent, A.M., Gupta, V., Georgescu, M., 2018. Diurnal interaction of urban expansion, climate change and adaptation in US cities. *Nat. Clim. Chang.* 8, 1097–1103. <https://doi.org/10.1038/s41558-018-0320-9>.
- Lai, A., Kwok, Y.T., Maing, M., Ng, E., 2018. Regression modelling of radiant fluxes on different view factors under shading in a densely built environment. *Archit. Sci. Rev.* 61, 15–28. <https://doi.org/10.1080/00038628.2017.1409614>.
- Lazzarini, M., Molini, A., Marpu, P.R., Ouara, T.B., Ghedira, H., 2015. Urban climate modifications in hot desert cities: the role of land cover, local climate, and seasonality. *Geophys. Res. Lett.* 42 (22), 9980–9989.
- Lee, H., Mayer, H., 2018. Thermal comfort of pedestrians in an urban street canyon is affected by increasing albedo of building walls. *Int. J. Biometeorol.* 62, 1199–1209. <https://doi.org/10.1007/s00484-018-1523-5>.
- Lee, H., Mayer, H., Schindler, D., 2014. Importance of 3-D radiant flux densities for outdoor human thermal comfort on clear-sky summer days in Freiburg, Southwest Germany. *Meteorol. Zeitschrift* 23, 315–330. <https://doi.org/10.1127/0941-2948/2014/0536>.
- Lindberg, F., Grimmond, C.S.B., 2011. The influence of vegetation and building morphology on shadow patterns and mean radiant temperatures in urban areas: model development and evaluation. *Theor. Appl. Climatol.* 105, 311–323. <https://doi.org/10.1007/s11252-011-0184-5>.
- Lindberg, F., Holmer, B., Thorsson, S., 2008. SOLWEIG 1.0 - modelling spatial variations of 3D radiant fluxes and mean radiant temperature in complex urban settings. *Int. J. Biometeorol.* <https://doi.org/10.1007/s00484-008-0162-7>.
- Lindberg, F., Holmer, B., Thorsson, S., Rayner, D., 2014. Characteristics of the mean radiant temperature in high latitude cities—implications for sensitive climate planning applications. *Int. J. Biometeorol.* 58, 613–627. <https://doi.org/10.1007/s00484-013-0638-y>.
- Lindberg, F., Onomura, S., Grimmond, C.S.B., 2016. Influence of ground surface characteristics on the mean radiant temperature in urban areas. *Int. J. Biometeorol.* 60, 1439–1452. <https://doi.org/10.1007/s00484-016-1135-x>.
- Luber, G., McGehee, M., 2008. Climate change and extreme heat events. *Am. J. Prev. Med.* 35, 429–435. <https://doi.org/10.1016/j.amepre.2008.08.021>.
- Mayer, H., Höppe, P., 1987. Thermal comfort of man in different urban environments. *Theor. Appl. Climatol.* 38, 43–49. <https://doi.org/10.1007/BF00866252>.
- Meehl, G.A., Tebaldi, C., 2004. More intense, more frequent, and longer lasting heat waves in the 21st century. *Science* 305, 994–997. <https://doi.org/10.1126/science.1098704>.
- Middel, A., Hüb, K., Brazel, A.J., Martin, C., Guhathakurta, S., 2014. Impact of urban form and design on mid-afternoon microclimate in Phoenix Local Climate Zones. *Landsc. Urban Plan* 122, 16–28. <https://doi.org/10.1016/j.landurbplan.2013.11.004>.
- Middel, A., Selover, N., Hagen, B., Chhetri, N., 2016. Impact of shade on outdoor thermal comfort—a seasonal field study in Tempe, Arizona. *Int. J. Biometeorol.* 60, 1849–1861. <https://doi.org/10.1007/s00484-016-1172-5>.
- Middel, A., Lukaszczuk, J., Maciejewski, R., 2017. Sky view factors from synthetic fisheye photos for thermal comfort routing—a case study in Phoenix, Arizona. *Urban Plan* 2 (1), 19. <https://doi.org/10.17645/up.v2i1.855>.
- Middel, A., Lukaszczuk, J., Zakrzewski, R., Demuzere, M., Roth, M., 2018. Sky View Factor footprints for urban climate modeling. *Urban Clim* 25, 120–134. <https://doi.org/10.1016/j.uclim.2018.05.004>.
- Middel, A., Lukaszczuk, J., Zakrzewski, S., Arnold, M., Maciejewski, R., 2019. Urban form and composition of street canyons: a human-centric big data and deep learning approach. *Landsc. Urban Plan* 183, 122–132. <https://doi.org/10.1016/j.landurbplan.2018.12.001>.
- Miller, N.L., Hayhoe, K., Jin, J., Auffhammer, M., 2008. Climate, extreme heat, and electricity demand in California. *J. Appl. Meteorol. Climatol.* 47, 1834–1844. <https://doi.org/10.1175/2007JAMC1480.1>.
- Oke, T.R., 1982. The energetic basis of the urban heat island. *Q. J. R. Meteorol. Soc.* (455), 1–24. <https://doi.org/10.1002/qj.49710845502>.
- Parsons, K., 2014. Human Thermal Environments: The Effects of Hot, Moderate, and Cold Environments on Human Health, Comfort, and Performance. CRC Press.
- Seto, K.C., Fragkias, M., Güneralp, B., Reilly, M.K., 2011. A meta-analysis of global urban land expansion. *PLoS One* 6 (8), e23777.
- Shashua-Bar, L., Pearlmutter, D., Erel, E., 2011. The influence of trees and grass on outdoor thermal comfort in a hot-arid environment. *Int. J. Climatol.* (10), 1498–1506. <https://doi.org/10.1002/joc.2177>.
- Stewart, I.D., Oke, T.R., Krayenhoff, E.S., 2014. Evaluation of the 'local climate zone' scheme using temperature observations and model simulations. *Int. J. Climatol.* 34 (4), 1062–1080.
- Steyn, D.G., 1980. The calculation of view factors from fisheye-lens photographs: research note. *Atmos. - Ocean.* 18, 254–258. <https://doi.org/10.1080/07055900.1980.9649091>.
- Thorsson, S., Lindberg, F., Eliasson, I., Holmer, B., 2007. Different methods for estimating the mean radiant temperature in an outdoor urban setting. *Int. J. Climatol.* 27, 1983–1993. <https://doi.org/10.1002/joc.1537>.
- Tucker, P., Gilliland, J., 2007. The effect of season and weather on physical activity: a systematic review. *Public Health* 121, 909–922. <https://doi.org/10.1016/j.puhe.2007.04.009>.
- USGCRP, 2018. In: Reidmiller, D.R., Avery, C.W., Easterling, D.R., Kunkel, K.E., Lewis, K.L.M., Maycock, T.K., Stewart, B.C. (Eds.), Impacts, Risks, and Adaptation in the United States: Fourth National Climate Assessment. vol. II. U.S. Global Change Research Program, Washington, DC, USA. <https://doi.org/10.7930/NCA4.2018>.
- VDI, 1998. Methods for the Human-Biometeorological Assessment of Climate and Air Hygiene for Urban and Regional Planning. Part 1: Climate. DI 3787, Part 2 (Berlin, 29p).
- Vespa, J., Armstrong, D.M., Medina, L., 2018. Demographic turning points for the United States: population projections for 2020 to 2060. *Current Population Reports, P25-1144* vol. 2018. U.S. Census Bureau, Washington, DC.
- Western Regional Climate Center, 2018. Climate norms. <http://www.wrcc.dri.edu/summary/Climsmaz.html>.
- Yaghoobian, N., Kleissl, J., Krayenhoff, E.S., 2010. Modeling the thermal effects of artificial turf on the urban environment. *J. Appl. Meteorol. Climatol.* 49, 332–345. <https://doi.org/10.1175/2009JAMC2198.1>.
- Zuo, J., Pullen, S., Palmer, J., Bennetts, H., Chileshe, N., Ma, T., 2015. Impacts of heat waves and corresponding measures: a review. *J. Clean. Prod.* 92, 1–12. <https://doi.org/10.1016/j.jclepro.2014.12.078>.